

Enhanced optical microlithography with a Fabry–Perot-based spatial filtering technique

Miklós Erdélyi, Zsolt Bor, William L. Wilson, Michael C. Smayling, and Frank K. Tittel

A coherent multiple imaging technique for use in optical microlithography was studied. The technique involves placing a thin Fabry–Perot etalon between the mask and the projection lens of an optical stepper. An optical lithographic computer simulation tool, Prolith/2, was used to evaluate the aerial image profile obtained for extended mask structures such as typical contact hole arrays and line–space patterns used in integrated circuit fabrication. Additionally, a set of experimental studies were performed to validate the simulation results. Enhancement of both resolution and depth of focus can be obtained simultaneously with appropriate etalon parameters. © 2000 Optical Society of America

OCIS codes: 110.4190, 070.6110, 110.4850, 100.2980, 110.5220.

1. Introduction

The need to reduce the minimum feature size in microelectronic devices at less than 150 nm requires optical techniques that improve resolution while maintaining depth of focus (DOF). The fundamental limits of optical lithography are described by the well-known Rayleigh scaling equations¹:

$$CD = k_1 \frac{\lambda}{\text{N.A.}}, \quad (1a)$$

$$\text{DOF} = k_2 \frac{\lambda}{\text{N.A.}^2}, \quad (1b)$$

where CD is critical dimension; λ is the exposure wavelength; N.A. is the numerical aperture (defined as the sine of the angular semiaperture in the image space) of the projection lens; and k_1 and k_2 are process- and system-dependent parameters, respectively. As efforts to reduce λ and increase N.A. encounter fundamental and economic barriers, new techniques for reducing k_1 and increasing k_2 have been developed. In the past 20 years several super-resolution techniques have been proposed. Four of

the most frequently studied methods include phase shifting, modified illumination, optical proximity correction, and multiple imaging. Phase-shifting technologies² based on constructive and/or destructive interference improve the image quality of different integrated circuit feature types. However, the fabrication and cleaning of phase-shifting masks is a costly and complicated processes that limits the applicability of phase-shifting techniques. Modified illumination techniques³ and control of spatial coherence have historically been used to optimize the performance of lithographic projection tools. The three-dimensional aerial image is influenced by the method of illumination. Off-axis, annular, and quadruple illuminations are the most extensively studied arrangements. Optical proximity correction⁴ aims at minimizing feature distortion, linewidth variation, and line-end shortening by predistortion of the patterns on the mask.

In this paper we focus on an alternative superresolution technique called coherent multiple imaging (CMI). CMI produces a series of images of the mask pattern, shifted in position along the optical axis. This is in contrast to a conventional projection process that produces only a single image at the wafer surface. Because the individual images are added together coherently, the final pattern is strongly dependent on the phase and the amplitude of each individual image.

Enhanced image formation by means of CMI has been investigated by several authors. The super-FLEX (focus latitude enhancement exposure) method reported by Fukuda *et al.*⁵ introduces a pupil-plane filter that creates two images with their focal planes

M. Erdélyi, W. L. Wilson, M. C. Smayling, and F. K. Tittel (fkt@rice.edu) are with the Department of Electrical and Computer Engineering, Rice University, 6100 Main Street, Houston, Texas 77251. Zs. Bor is with the Department of Optics and Quantum Electronics, József Attila Tudományegyetem (JATE) University, H-6720 Szeged, Dóm tér 9, P.O. Box 406, Hungary

Received 16 August 1999.

0003-6935/00/071121-09\$15.00/0

© 2000 Optical Society of America

shifted by $\pm\beta$ and their phases shifted by $\pm\varphi$. The resultant pattern is the superposition of these two images. Experimental and theoretical results have shown that, for a contact hole pattern, the super-FLEX technique is capable of enhancing the DOF by a factor of 3 and the resolution by 20%. A CMI technique that uses a Fabry–Perot etalon placed between the mask and the optical stepper projection lens has been demonstrated both theoretically⁶ and experimentally.⁷ In this approach an etalon generates multiple virtual images of the mask in front of the lens, separated by $2d$ along the optical axis, where d is the separation of the etalon mirrors. The projection lens then creates an aerial image that is a superposition of all the shifted virtual mask images. The separation of the images along the optical axis beyond the lens is $2dM^2$, where M^2 is the longitudinal magnification of the lens. It was demonstrated that an optimized etalon could enhance the depth of focus and the resolution of a single on-axis contact hole by 300% and 60%, respectively.⁷ However, in Ref. 6, calculations for extended mask patterns were not possible, owing to the limitations of the wave optics model that was used.

Recently, it was shown that a simple and fast simulation technique could be applied to the CMI approach for extended mask images by use of an appropriate pupil-plane filter in the simulator.⁸ The thrust of the current study is a comparative experimental and theoretical evaluation of the above-mentioned CMI technique for contact hole arrays and line-space patterns. A commercially available microlithographic simulation tool, Prolith/2, was used to calculate the aerial images of such mask structures for various structure sizes and DOF's.

2. Fabry–Perot Interferometer as a Pupil-Plane Filter

A Fabry–Perot interferometer placed between the mask and the projection lens of an optical stepper can be considered to be a spatial filter that transmits certain spatial Fourier components of the mask pattern while blocking others.^{8–10} On the basis of this analogy, the etalon can be substituted by a pupil-plane filter that can be introduced into any commercially available photolithographic simulation tool (Prolith/2, Solid-C, Depict, and the like) without software modifications. The principle of image formation based on Fourier optics can be summarized as follows. The electric field pattern in the focal plane, $E(x, y)$, is given by

$$E(x, y) = \mathcal{F}^{-1}\{\mathcal{F}\{m(x, y)\}P(f_x, f_y)\}, \quad (2)$$

where $m(x, y)$ is the electric field transmittance of the mask pattern; $P(f_x, f_y)$ is the coherent transfer function of the stepper optical configuration; and \mathcal{F} and \mathcal{F}^{-1} represent the Fourier and the inverse-Fourier transforms, respectively. The coherent transfer function describes the optical imaging system. This function specifies all the information about the imaging system including optical aberrations, defocus,

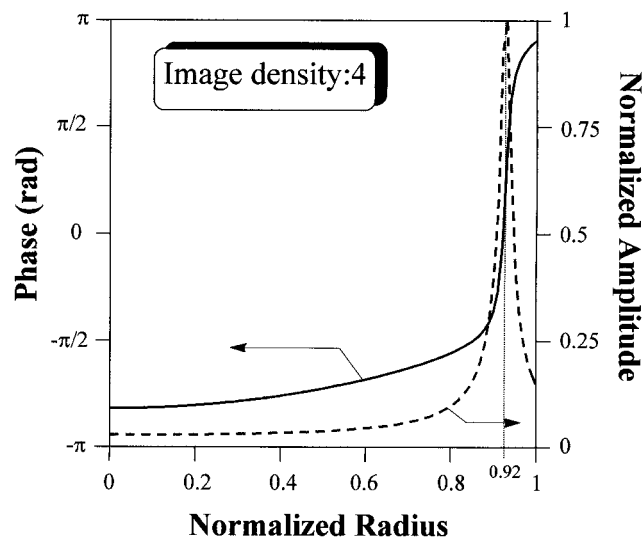


Fig. 1. Normalized amplitude and phase distribution of the pupil-plane filter that was used to simulate a Fabry–Perot etalon with $d = 122 \mu\text{m}$ and $R = 0.97$.

N.A., and pupil-plane filters, which is necessary for calculating the aerial image.

For a Fabry–Perot filter with spacing d , and mirror reflectivity R , the images created by the projection lens with magnification M are shifted by $2dM^2, 4dM^2, 6dM^2, \dots$. The phase is shifted by $\varphi, 2\varphi, 3\varphi, \dots$, where φ depends on the exact mirror spacing in the etalon. The amplitude ratio between the adjacent images is simply given by R , the reflectivity of the mirrors. The total electric field is the superposition of these images. The modified pupil-plane filter that simulates the effect introduced by a Fabry–Perot etalon can be expressed as follows:

$$P(r) = -R \exp(-i\Phi) \frac{1}{R \exp(-i\Phi) - 1}, \quad (3)$$

$$\Phi = \phi - 2\pi \left(\frac{2}{\text{N.A.}^2} + r^2 \right) 2dM^2, \quad (4)$$

and r is the normalized pupil radius. This phase-amplitude filter can be defined by means of a projection lens pupil filter file in Prolith/2. The main advantages of this simulation approach are the following:

- Simulation of extended mask structures becomes feasible.
- A single simulation run is required instead of multiple runs.
- No software modifications are required.

Figure 1 depicts the amplitude and phase properties of the filter that is studied theoretically and experimentally in this paper. The input stepper parameters for the Prolith simulation are as follows:

- Image calculation mode, full scalar.¹¹

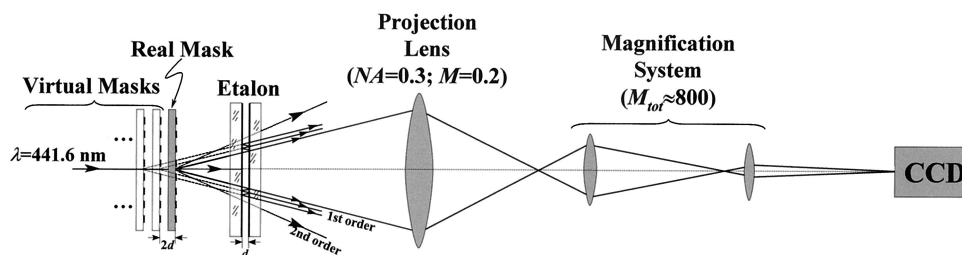


Fig. 2. Schematic view of the experimental arrangement. The Fabry–Perot etalon placed between the mask and the projection lens creates multiplied images of the mask pattern along the optical axis. The projection lens images all the virtual patterns simultaneously. The final superimposed image is magnified by two microscope objectives and is captured by a CCD camera.

- N.A., 0.3.
- Wavelength, 441.6 nm (cw He–Cd laser).
- Reduction ($1/M$), 5.
- Spatial coherence (σ), 0.

The DOF and the resolution limits of this system with the Rayleigh equations are $\text{DOF} = 2\lambda/\text{N.A.}^2 = 9.8 \mu\text{m}$ and $\text{CD} = 0.61 \lambda/\text{N.A.} = 0.9 \mu\text{m}$.

The pupil-plane filter depicted in Fig. 1 represents a Fabry–Perot etalon with a mirror separation of $d = 122 \mu\text{m}$ and a mirror reflectivity of $R = 0.97$. The relative image density, N , defined by the number of images in one DOF range, ($N = \text{DOF}/2dM^2$) beyond the projection lens is 4. The filter is optimized so that the amplitude transmission maximum is close to the edge of the aperture (the relative radius position of the main peak is 0.92). The phase changes rapidly where the filter transmits the incident light. This special phase property of the filter introduces a focal shift along the optical axis, as discussed below. Since the reflectivity of the mirrors is high, and the relative image density is relatively small, the transmission ring of the filter is sharp.

3. Experimental Arrangement

A schematic view of the experimental arrangement is depicted in Fig. 2. The experimental and the simulation parameters were identical. The projection lens available for this study was a Tropel stepper lens (5116g) optimized for g line (436-nm) stepper illumination with N.A. = 0.3 and $M = 0.2$. The image field diameter of the lens was 20 mm, and the object-to-image distance was 800 mm. Because of the large image field diameter of the lens, aberrations introduced by off-axis patterns were essentially eliminated. The chrome mask contained different line-space and contact hole patterns and was illuminated by a cw He–Cd laser operating at 441.6 nm. The choice of illumination wavelength used in this study was determined by the availability of suitable optics and diagnostic equipment. All of the results obtained here can be scaled to shorter wavelengths, i.e., deep-ultraviolet excimer wavelengths. A scanning Fabry–Perot etalon (Tropel C.L.-100) was placed between the mask and the projection lens. The reflectance of the etalon mirrors was $R = 0.97$ at 441.6 nm, and the mirror separation was set at $122 \mu\text{m}$. We controlled and checked the mirror separation several

times during the experiment by measuring the radii of the Fabry–Perot rings. The final image produced by the projection lens was magnified by two microscope objectives and captured by a CCD camera. The total magnification in front of the CCD was approximately $40 \times 20 = 800\times$. The exact value of magnification was calibrated by means of the pitch size of the largest pattern on the mask. The first objective was mounted on a precision translation stage so that the image could be evaluated as a function of focal position.

4. Simulation and Experimental Results

A. Contact Hole Arrays

Images of contact hole arrays without and with the Fabry–Perot filter were studied. A schematic view of the mask pattern used in these investigations is depicted in Fig. 3. Since the pattern is periodic, the figure depicts only a portion of the mask. All the masks contain $10 \times 10 = 100$ contact holes in the form of an offset pattern. The CD varied from 1.0 to $0.52 \mu\text{m}$ in steps of $0.08 \mu\text{m}$, whereas the pitch/hole size ratio remained constant. In fact, such an offset hole array can be considered to be a conventional hole

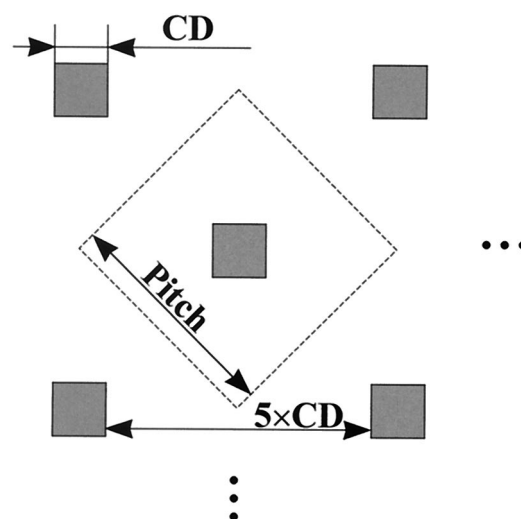


Fig. 3. Offset contact hole array. The CD varies from 1.0 to $0.52 \mu\text{m}$ in steps of $0.08 \mu\text{m}$, whereas the pitch/CD size ratio remains constant.

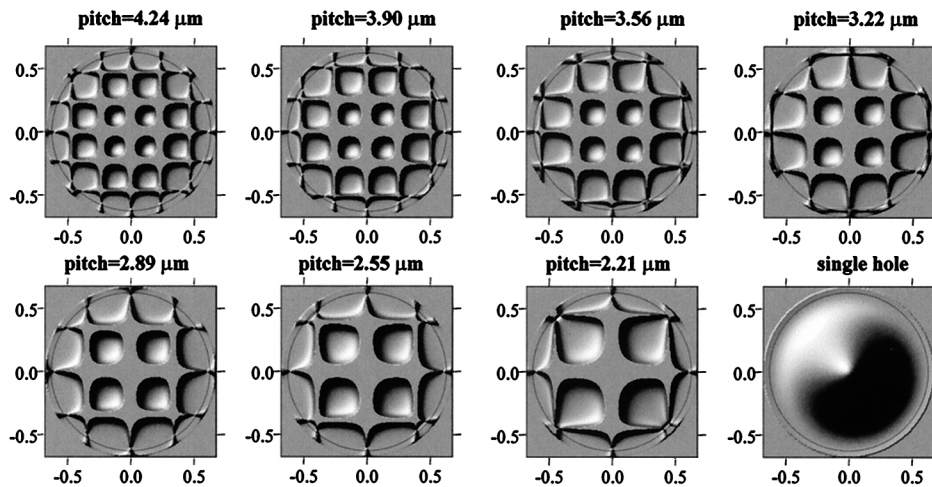


Fig. 4. Intensity distribution in the pupil-plane using contact hole arrays with different pitch size.

array tilted by 45° , if the optical system is cylindrically symmetric. The pitch sizes of the contact holes changed from 4.24 to $2.21 \mu\text{m}$. The two-dimensional Fourier transforms that correspond to the intensity distribution in the pupil plane of the masks are depicted in Fig. 4. The circles drawn in each panel mark the position of the transmission maximum of the Fabry-Perot filter. The figure also depicts the intensity distribution in the pupil plane when a single on-axis contact hole was used. The maximum spatial frequency component transmitted by the lens is determined by the N.A. of the lens and the illumi-

nation wavelength ($\nu_{\text{max}} = \text{N.A.}/\lambda = 0.68 \mu\text{m}^{-1}$). The quality of an imaged contact hole array is determined by the number of Fourier components transmitted by the projection lens. Without the filter, for a given wavelength, the N.A. determines the highest Fourier frequency (ν_{max}) that can contribute to the imaging process. Figure 4 shows that the smaller the pitch size on the mask, the larger the diffraction angle and hence the spatial separation of the diffraction orders. An image cannot be resolved if only the zero diffraction order passes through the lens. All the patterns depicted in Fig. 4 can be resolved, since

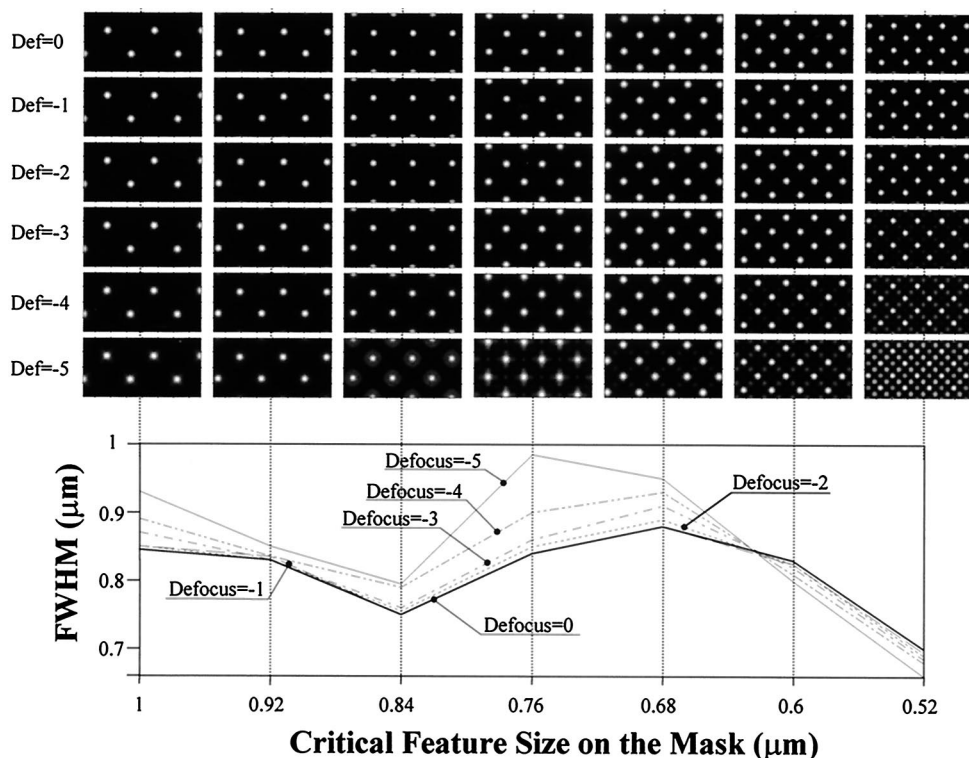


Fig. 5. Two-dimensional simulation results through focus without filter. The depicted size of the aerial images is $7.5 \mu\text{m} \times 15 \mu\text{m}$. The value of defocus (Def) gives the distance between the examined and the focal plane.

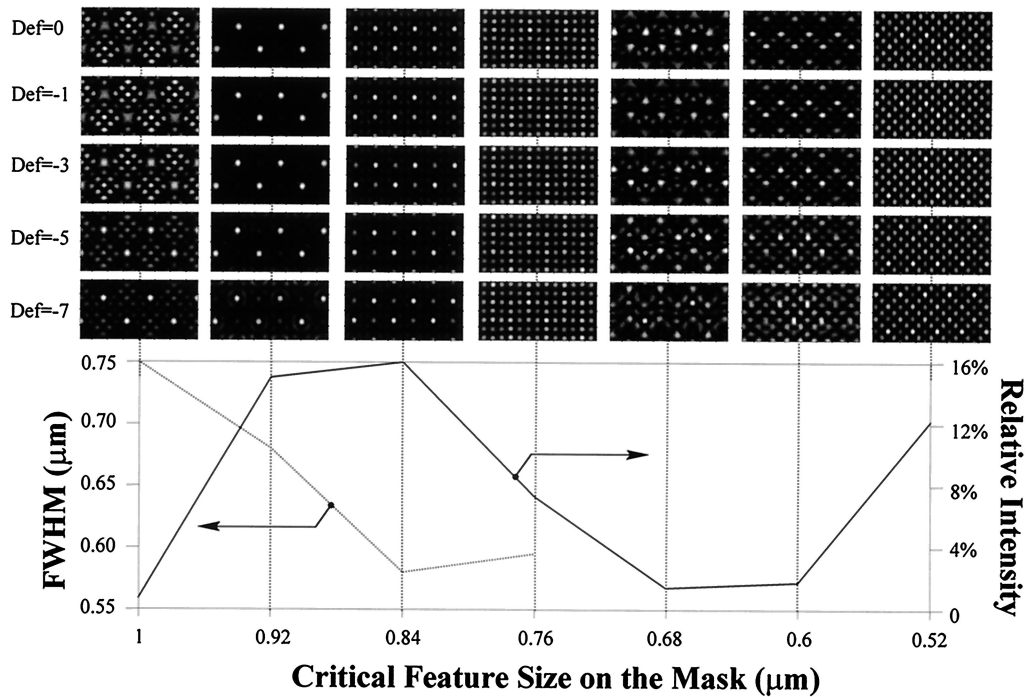


Fig. 6. Two-dimensional simulation results through focus with filter. The characteristics of the aerial images of patterns with different CD's vary but do not change with focal position. In the case of pitch size at 0.84 μm the second diffraction orders are transmitted by the Fabry-Perot filter. This is the optimum case from the standpoint of both intensity loss and resolution.

at least the zero order and first diffraction orders occur inside the aperture. However, the DOF and the resolution (measured by the FWHM of the intensity peaks) strongly vary with pitch size. Figure 5 shows the simulated aerial images and the FWHM of the peaks for the seven masks at different focal positions. The depicted size of the aerial images is $7.5 \mu\text{m} \times 15 \mu\text{m}$. The FWHM dependence on the CD is similar

for different values of defocus. A noticeable change in FWHM and DOF can be observed when the critical feature size falls below 0.84 μm . This phenomenon is explained in Fig. 4. Below a CD of 0.84 μm (equivalent to 3.56- μm pitch size) the ± 2 diffraction orders fall outside the aperture, and they do not contribute to the final image. Therefore the FWHM increases rapidly while the DOF decreases. If the CD is re-

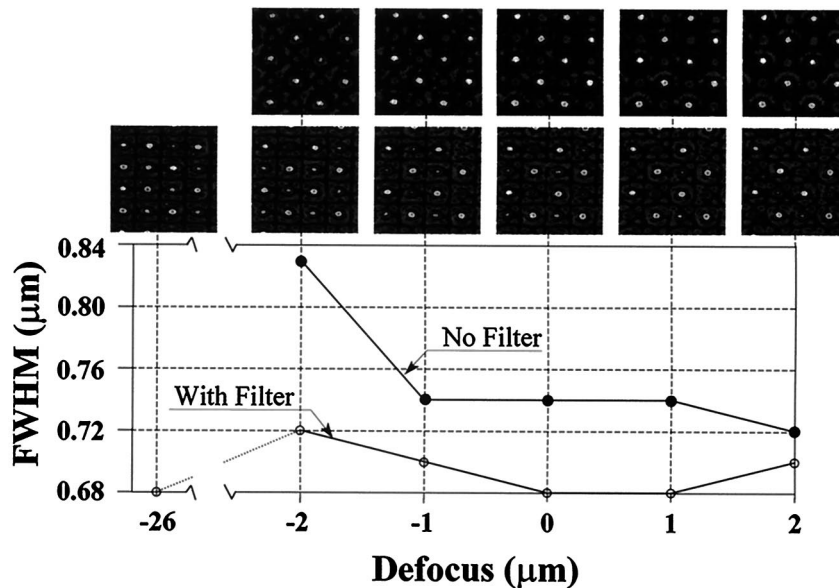


Fig. 7. Experimental results without (upper row) and with (lower row) filter through focus. The filter decreases the FWHM by 8%. However, the increased intensity side lobes cause undesirable interference effects. When the defocus is 8 μm , the intensities of the secondary and the main peaks become equal.

duced further, the first diffraction orders get closer to the edge of the aperture, resulting in improved resolution.

A narrow-band pupil-plane filter introduces a strong modification of the Fourier components, and the system becomes extremely pitch sensitive. Only Fourier components that pass through the narrow transmission peak of the filter can contribute to the final image. The simulated aerial images, obtained by means of the pupil-plane filter defined in the Section 3 can be seen in Fig. 6. The characteristics of the aerial images of patterns with different CD's vary but do not change with focal position; i.e., the DOF has improved significantly. At the same time, the FWHM has decreased from 0.75 to 0.58 μm ($\approx 22\%$ resolution enhancement), using the pattern with a 0.84- μm CD. This is the optimum case not only from a resolution standpoint but also in terms of minimizing light loss. The Strehl ratio (which is defined as the intensity ratio of the aerial images in the presence and in the absence of optical aberrations) is $\sim 16\%$. In this case the second diffraction orders are transmitted by the Fabry-Perot filter. If we further decrease the CD, then the diffraction angles of the second orders increase and are not transmitted by the filter. The intensity drops drastically, and images cannot be evaluated.

Patterns similar to those that were used in the simulation studies were also evaluated experimentally, with the setup described above. The images were captured by the CCD camera, and the FWHM was determined for each focal position. The detailed experimental evaluation of the optimum pattern with a CD = 0.84 μm can be seen in Fig. 7. The upper and the lower rows depict the captured CCD images without and with the filter, respectively. Without the filter, the FWHM of the main peaks is 0.74 μm and the DOF is approximately 3–4 μm . The filter decreases the FWHM by 8% (from 0.74 to 0.68 μm) at optimum focus. The thick Fabry-Perot mirror substrates introduce a constant focal shift. Therefore the zero defocus with and without the etalon does not represent the same physical position. Thus zero defocus is defined as the position where the best image can be formed. The $-4\text{-}\mu\text{m}$ focus shift caused by the pupil-plane filter is significantly smaller than the defocus of several millimeters introduced by the thick mirror substrates.

There is, however, a secondary effect associated with the use of a Fabry-Perot filter for imaging contact hole arrays. This is the appearance of diffraction rings and their undesirable interference effects. Even in the best focal plane the intensity of the secondary maxima between the main peaks is 40% and increases with defocus. When the defocus is 8 μm , the intensities of the secondary and the main peaks become equal. Figure 7 also depicts a CCD image when the defocus is $-26\text{ }\mu\text{m}$. The FWHM of the main peaks does not change, but the secondary peaks are higher than the main peaks. A detailed evaluation of the simulation and the experimental results shows that the high-intensity secondary peaks are

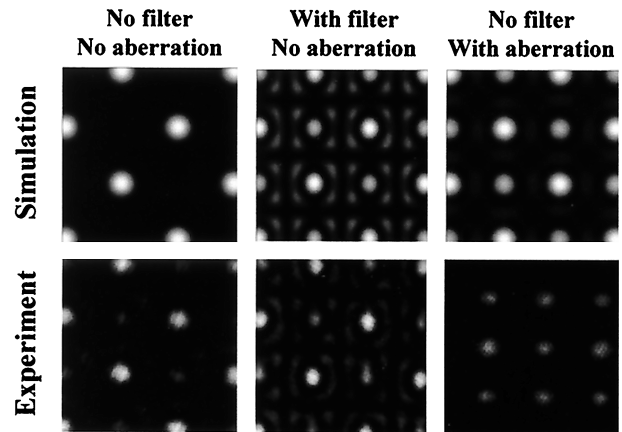


Fig. 8. High-intensity secondary maxima generated by filter and optical aberrations.

generated by four completely overlapping second diffraction rings. However, high-intensity side lobes are generated not only by the filter but also by optical aberrations in the stepper projection system. Simulation and experimental results depicted in Fig. 8 show that aberration can cause even higher secondary peaks than with the filter. During simulation a typical, predefined aberration file was used to introduce a small aberration into the optical system.

Two methods are proposed to avoid this undesirable interference effect.⁸ The first method changes the spatial coherence of the illumination. The optimum value of spatial coherence, in terms of minimizing the sidelobe interference, was found to be 0.28. The other method, based on a phase-shift approach, introduces a π phase shift between adjacent holes. Because of the destructive interference between opposite fields, the secondary maxima will disappear. However, it was not possible to observe this effect with our experimental apparatus.

B. Line-Space Patterns

Besides contact hole arrays, the other key patterns in optical microlithography are line-space patterns. This subsection describes the evaluation of nine line-space patterns with different pitches but with the same pitch/CD ratio. The pitch is changed in the range of 2 to 1.36 μm in steps of 0.08 μm , and the width of the lines is equal to their separations so that the pitch/CD ratio is 2. Every pattern contains ten lines with a length of 10 μm . The two-dimensional Fourier transforms of eight patterns can be seen in Fig. 9. As the pitch is decreased, the diffraction angle of the ± 1 orders increases. With a conventional illumination system a line-space pattern can be imaged if at least three diffraction orders contribute to the final image. Since the position of the zero order does not change, the position of the ± 1 diffraction orders determines the resolution limit. However, the diffraction angle depends only on the wavelength/pitch ratio and is independent of the width of the lines. Figure 9 shows that the line-space patterns with 1.52- μm or larger pitches can be resolved,

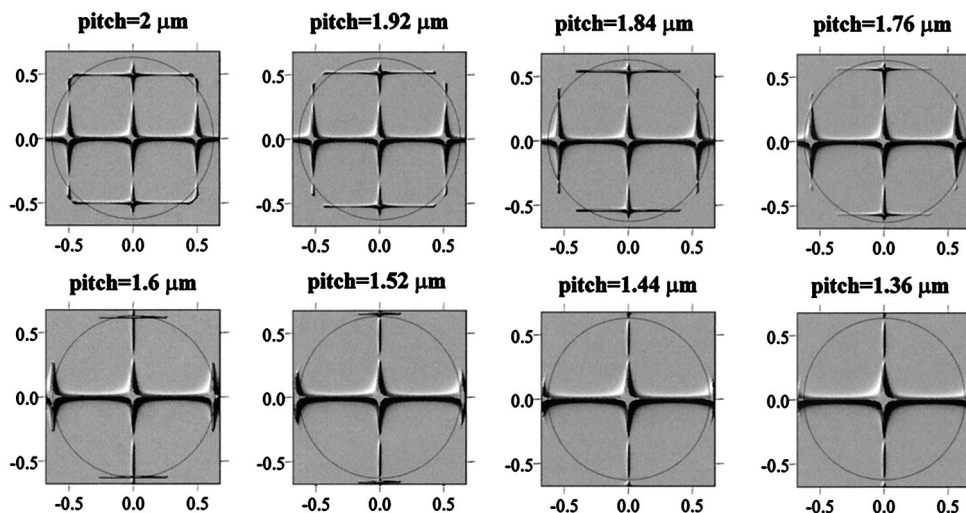


Fig. 9. Intensity distribution in the pupil-plane using line-space patterns with different pitch size.

whereas the 1.44- μm pattern is below the resolution limit of the lens. This result is in good agreement with a simple geometrical model that determines that the minimum resolvable pitch size ($\lambda/\text{N.A.}$) is 1.47 μm . The position of the amplitude maximum of the filter is also shown in Fig. 9.

The simulated and the experimental aerial images of the nine line-space patterns in the optimum focal plane (defocus, 0) obtained without a filter can be seen in Fig. 10. The simulation results (upper row) agree with the experimental results (lower row). The line-space feature with a 1.52- μm pitch is the smallest resolvable pattern. Above the resolution limit both the pitch and FWHM results follow theo-

retical values. The gradient of the FWHM curve is half the pitch curve. The normalized intensity curves show that the peak intensities do not change significantly above the resolution limit. However, by use of patterns with smaller pitches, the FWHM of the lines starts to increase, and the peak intensity decreases rapidly.

The simulated and the experimental aerial images generated with the use of the pupil-plane filter can be seen in Fig. 11. The filter shifts the intensity maximum toward the lens by 5 μm . Therefore both the simulation and the experimental data depicted in Fig. 11 were obtained by introduction of a -5- μm defocus. The presence of the pupil-plane filter

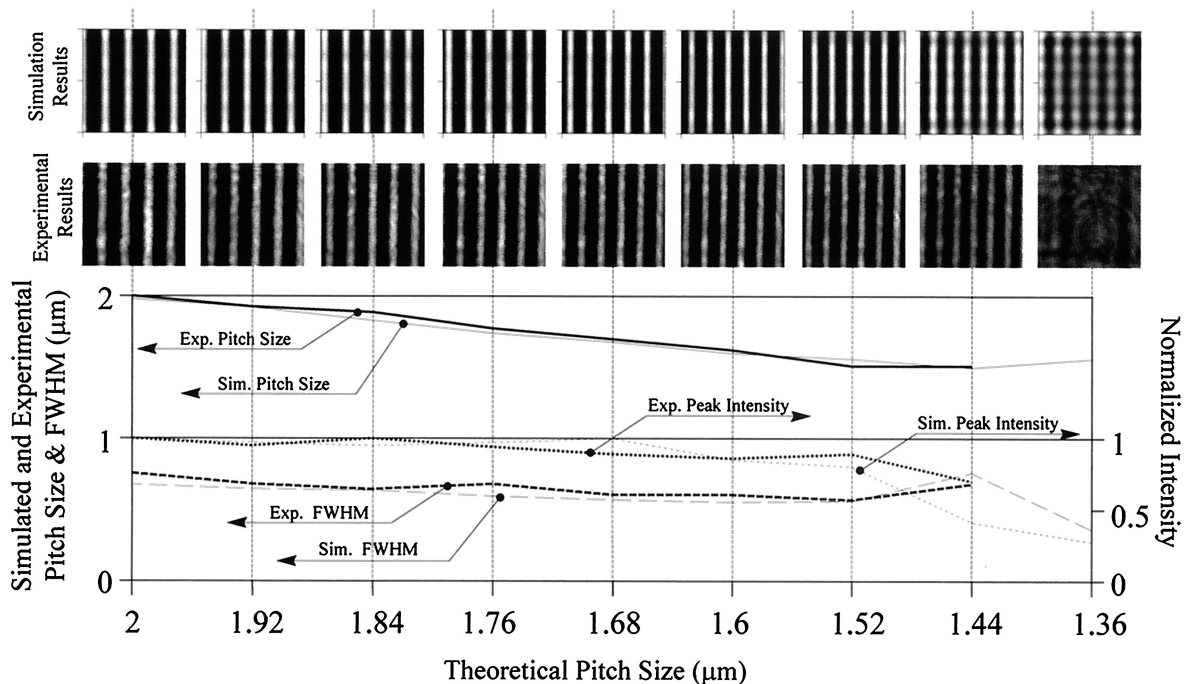


Fig. 10. Simulation results and experimental results of line-space patterns without filter (defocus, 0). The resolution limit of the optical system is pitch size at 1.52 μm .

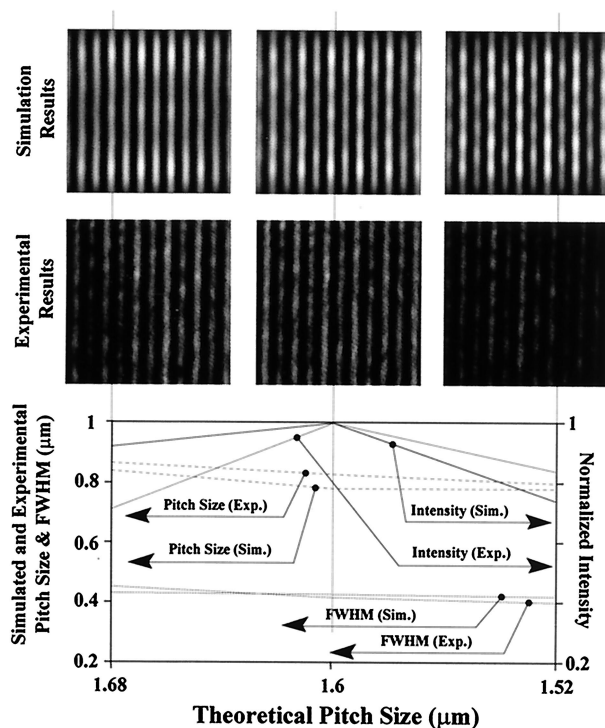


Fig. 11. Simulation results and experimental results with the Fabry-Perot filter (defocus, $-5 \mu\text{m}$). The periods of the patterns are doubled, since the filter blocks the zero order.

changes the aerial image significantly. The zero diffraction order is always blocked by the Fabry-Perot filter, and hence the angle between the diffraction orders generating the final image is doubled. Because of this, the period of the generated pattern is also doubled. It is important to note that the doubled periodicity is caused by the missing zero order and not by an interference effect between the “real” lines.

Because of the narrow bandwidth of the filter, the system is pitch sensitive. A line-space pattern can be projected if its first diffraction orders can be transmitted by the filter. This is why Fig. 11 shows only three patterns. For any other pattern the filter blocks all the diffraction orders. By use of a pattern with $1.6\text{-}\mu\text{m}$ pitch the amplitude maximum of the filter matches the first diffraction orders of the pattern. This is an optimum case, as far as filter transmission is concerned. The peak intensities of the adjacent patterns (for pitches of 1.68 and $1.52 \mu\text{m}$) decrease rapidly. The FWHM of the lines is decreased by 25% (from 0.56 to $0.42 \mu\text{m}$).

The aerial image of the optimum line-space pattern ($1.6\text{-}\mu\text{m}$ pitch) was also evaluated with different defocus values. The first and the second rows in Fig. 12 depict the simulation results and the experimental results when no filter is used. Since the intensity distribution is symmetrical with respect to the focal

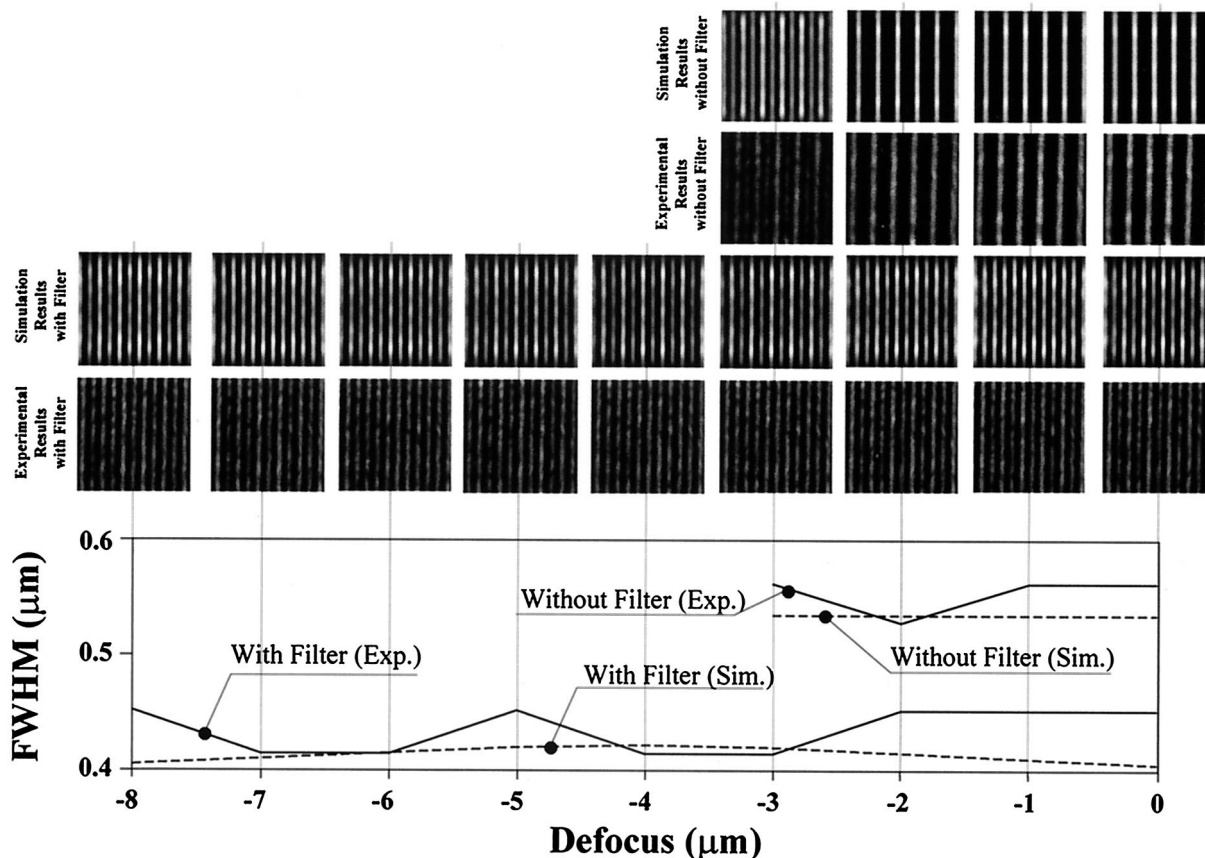


Fig. 12. Simulation results and experimental results in the presence and in the absence of the Fabry-Perot filter with line-space pattern of $1.6\text{-}\mu\text{m}$ pitch. The filter significantly increases the depth of focus and enhances the resolution.

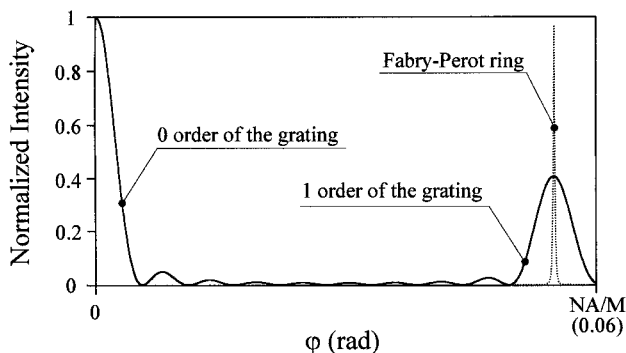


Fig. 13. Source of light loss. The narrow Fabry-Perot transmission ring could transmit only a part of the first diffraction order.

point, the figure shows only the defocus range from -3 to $0\ \mu\text{m}$. The DOF is $\approx 4\ \mu\text{m}$. The third and the fourth rows depict the simulation results and the experimental results with the Fabry-Perot filter inserted into the optical system. It can be seen that the DOF of the doubled periodicity pattern is increased significantly. As the experimental results show, the filter increased the DOF by a factor of ~ 9 while maintaining a 25% enhancement in FWHM.

The filter with a narrow bandwidth introduces both a pitch sensitivity and light loss into the optical system. Since the bandwidth of the filter is narrower than the width of the first diffraction order, the filter transmits only a fraction of the light contained there. The Fabry-Perot ring and the diffraction orders (zero and first orders) can be seen in Fig. 13. The figure represents an optimum case, in which the Fabry-Perot ring is in the middle of the first order. The simulation results and the experimental results show that the peak intensity decreases to $\sim 4\%$ of the original maximum when the Fabry-Perot filter is used. This significant light loss can be avoided by means of a Fabry-Perot etalon with lower reflectivity mirrors. For an optimum case, the bandwidth of the filter would be set equal to the width of the first diffraction order so that the filter transmits the ± 1 diffraction orders, and the peak intensity will reach 30% of the original maximum.

5. Conclusions

A coherent multiple imaging technique applied to both contact hole arrays and line-space patterns has been evaluated theoretically and experimentally. A computer simulation method based on Prolith/2 was developed that is able to analyze the effect of a Fabry-Perot etalon inserted into a commercial lithographic exposure tool. This method is based on using a pupil-plane filter to simulate the effect of a Fabry-Perot filter placed after the projection lens in a photolithographic stepper. An experimental test bench was also developed to verify the simulation results and to demonstrate real-world feasibility.

The results obtained from the simulations agreed well with the experimental results. It was demonstrated that, under certain conditions, the use of a Fabry-Perot filter can simultaneously improve both resolution and depth of focus. The results showed that the resolution and the DOF could be enhanced by 25–29% and 300–900%, respectively, depending on the selected pattern. The strong pitch sensitivity and high-intensity side lobes introduced by the etalon were analyzed, and two methods were proposed to avoid their undesirable interference effects.

This research was supported in part by the University Research Program of Texas Instruments, Inc., and by the Országos Tudományos Kutatási Alap (OTKA) Foundation of the Hungarian Academy of Sciences (T020910) and Felsőoktatási Kutatási és Fejlesztési Pályázat (FKFP) (1239/1997). We thank Chris Mack of FINLE Technologies for making Prolith/2 available to this study.

References

1. M. Born and E. Wolf, *Principles of Optics*, 6th ed. (Pergamon, New York, 1980).
2. M. D. Levenson, "Extending the lifetime of optical lithography technologies with wavefront engineering," *Jpn. J. Appl. Phys.* **33**, 6765–6773 (1994).
3. H. J. Levinson and W. H. Arnold, eds., *Handbook of Microlithography, Micromachining, and Microfabrication. Volume 1: Microlithography*, Vol. PM39 of SPIE Press Monographs and Handbooks (SPIE, Bellingham, Wash., 1997), p. 71.
4. J. F. Chen, T. Laidig, K. E. Wampler, and R. Caldwell, "Full-chip optical proximity correction with depth of focus enhancement," *Microlithography World* **6**(3), 5–13 (1997).
5. H. Fukuda, T. Terasawa, and S. Okazaki, "Spatial filtering for depth of focus and resolution enhancement in optical lithography," *J. Vac. Sci. Technol. B* **9**, 3113–3116 (1991).
6. Z. L. Horváth, M. Erdélyi, G. Szabó, Zs. Bor, F. K. Tittel, and J. R. Cavallaro, "Generation of nearly nondiffracting Bessel beams with a Fabry-Perot interferometer," *J. Opt. Soc. Am. A* **14**, 3009–3013 (1997).
7. M. Erdélyi, Z. L. Horváth, G. Szabó, Zs. Bor, F. K. Tittel, J. R. Cavallaro, and M. C. Smayling, "Generation of diffraction-free beams for applications in optical microlithography," *J. Vac. Sci. Technol. B* **15**, 287–292 (1997).
8. M. Erdélyi, Zs. Bor, W. L. Wilson, M. C. Smayling, and F. K. Tittel, "Simulation of coherent multiple imaging by means of pupil plane filtering in optical microlithography," *J. Opt. Soc. Am. A* **16**, 1909–1914 (1999).
9. M. Erdélyi, A. Kroyan, K. Osvay, Zs. Bor, W. L. Wilson, M. C. Smayling, and F. K. Tittel, "Coherent multiple imaging by means of pupil plane filter," in *Optical Microlithography XII*, L. Van den Hove, ed., SPIE Proc. **3679**, 762–771 (1999).
10. M. Erdélyi, K. Osvay, Zs. Bor, W. L. Wilson, M. C. Smayling, and F. K. Tittel, "Enhanced microlithography using coherent multiple imaging, international symposium on microelectronics manufacturing technologies, in *Lithography for Semiconductor Manufacturing*, C. A. Mack and T. Stevenson, eds., Proc. SPIE **3741**, 180–188 (1999).
11. C. Mack, *Inside Prolith: A Comprehensive Guide to Optical Lithography Simulation* (FINLE Technologies Inc., Austin Tex., 1997).